

OPEN ACCESS

UTILE-Pore: Deep Learning-Enabled 3D Analysis of Porous Materials in Polymer Electrolyte Membrane-Based Energy Devices

To cite this article: André Colliard-Granero *et al* 2025 *J. Electrochem. Soc.* **172** 074515

View the [article online](#) for updates and enhancements.

You may also like

- [Quasi-Solid State and Hybrid Zinc Ion Photo-Supercapacitors Based on Manganese Oxide Nanostructures](#)
Tuluhan Olcayto Colak, Ecenaz Yaman, Cigdem Tuc Altat et al.
- [Effect of \$Mg^{2+}\$ Ions on Galvanic Corrosion of Linear Friction Welded Magnesium AZ91 Alloy - Aluminum AA6061 Alloy](#)
Isao Nakatsugawa, Mingzhe Bian, Ryoichi Furushima et al.
- [High-Performance Metal Free rGO-Benzothiazole Hybrid Electrode for Simultaneous Sensing of Dopamine and Paracetamol](#)
Randeep Kaur, Shweta Rana, Hitakshi Singh et al.

ECC-Opto-10 Optical Battery Test Cell: Visualize the Processes Inside Your Battery!

EL-CELL®
electrochemical test equipment

- ✓ **Battery Test Cell for Optical Characterization**
Designed for light microscopy, Raman spectroscopy and XRD.
- ✓ **Optimized, Low Profile Cell Design (Device Height 21.5 mm)**
Low cell height for high compatibility, fits on standard samples stages.
- ✓ **High Cycling Stability and Easy Handling**
Dedicated sample holders for different electrode arrangements included!
- ✓ **Cell Lids with Different Openings and Window Materials Available**



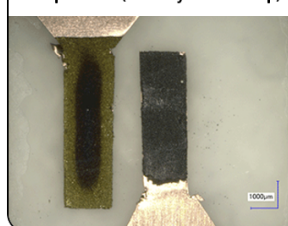
Contact us:

+49 40 79012-734

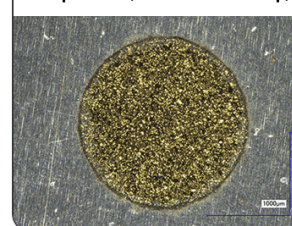
sales@el-cell.com

www.el-cell.com

Sample Test (Side-by-Side Setup)



Sample Test (Face-to-Face Setup)





UTILE-Pore: Deep Learning-Enabled 3D Analysis of Porous Materials in Polymer Electrolyte Membrane-Based Energy Devices

André Colliard-Granero,^{1,2,*} Salvatore Ranieri,³ Aimy Bazylak,^{3,*} Tobias Morawietz,⁴ K. Andreas Friedrich,^{4,5} Jasna Jankovic,⁶ Michael H. Eikerling,^{1,2,7,*} Kourosh Malek,^{1,2,*} and Mohammad J. Eslamibidgoli^{1,2,z}

¹Theory and Computation of Energy Materials (IET-3), Institute of Energy Technologies, Forschungszentrum Jülich GmbH, 52425 Jülich, Germany

²Centre for Advanced Simulation and Analytics (CASA), Simulation and Data Science Lab for Energy Materials (SDL-EM), Forschungszentrum Jülich GmbH, 52425 Jülich, Germany

³Bazylak Group, Department of Mechanical & Industrial Engineering, Faculty of Applied Science and Engineering, University of Toronto, M5S 3G8 Toronto, Canada

⁴Institute of Engineering Thermodynamics, German Aerospace Center (DLR), 70569 Stuttgart, Germany

⁵University of Stuttgart, Institute of Building Energetics, Thermal Engineering and Energy Storage (IGTE), 70569 Stuttgart, Germany

⁶Center for Clean Energy Engineering, University of Connecticut, Storrs, Connecticut 06269, United States of America

⁷Chair of Theory and Computation of Energy Materials, Faculty of Geosciences and Materials Engineering, RWTH Aachen University, 52062 Aachen, Germany

3D imaging of porous materials in polymer electrolyte membrane (PEM)-based devices, coupled with in situ diagnostics and advanced multi-scale modelling approaches, is pivotal to deciphering the interplay of mass transport phenomena, performance, and durability. The characterization of porous electrode media in PEM-based cells encompassing gas diffusion layers and catalyst layers often relies on traditional analytical techniques such as 2D scanning electron microscopy, followed by image processing such as Otsu thresholding and manual annotation. These methods lack the 3D context needed to capture the complex physical properties of porous electrode media, while also struggling to accurately and effectively discriminate porous and solid domains. To achieve an enhanced, automated segmentation of porous structures, we present a 3D deep learning-based approach trained on calibrated 3D micro-CT, focused ion beam-scanning electron microscopy datasets, and data from physical porosity measurements. Our approach includes binary segmentation for porous layers and a multiclass segmentation method to distinguish the microporous layers from the gas diffusion layers. The presented analysis framework integrates functions for pore size distribution, porosity, permeability, and tortuosity simulation analyses from the resulting binary masks and enables quantitative correlation assessments. Segmentations achieved can be interactively visualized on-site in a 3D environment.

© 2025 The Author(s). Published on behalf of The Electrochemical Society by IOP Publishing Limited. This is an open access article distributed under the terms of the Creative Commons Attribution 4.0 License (CC BY, <https://creativecommons.org/licenses/by/4.0/>), which permits unrestricted reuse of the work in any medium, provided the original work is properly cited. [DOI: 10.1149/1945-7111/adf262]



Manuscript submitted May 14, 2025; revised manuscript received July 15, 2025. Published July 31, 2025.

Electrochemical energy technologies that utilize polymer electrolyte membranes (PEMs), e.g., polymer electrolyte fuel cells (PEFCs) and water electrolyzers (PEWEs), offer high current densities, minimal reactant crossover, and volumetrically compact designs, making them a promising option for hydrogen generation and conversion as compared to conventional alkaline systems, which typically operate at lower current densities and suffer from higher gas crossover rates.^{1–3} Nonetheless, the high costs associated with precious metal catalysts and the need for enhanced mass transport remain significant barriers to broader commercialization. These issues are especially prevalent in both the catalyst layer (CL) and the gas diffusion layer (GDL), two main components in PEFC and PEWE electrodes. For this reason, understanding how their function and structures are related is critical for describing transport properties such as thermal and electrical conductivity, as well as improving cell performance and degradation.^{4–7}

The electrode layers in these cells are highly porous and exhibit a multi-scale characteristic length progression from a few nanometers within the CL to tens of microns within the GDL substrate, which supports a hierarchy of functions to minimize voltage losses of these cells. For instance, GDL porosity plays a critical role in governing reactant transport towards the CL while maintaining humidity, directly affecting the mass transport and proton conductivity, respectively.^{8,9} On the other hand, within the CL, the porosity spans lengths from several to tens of nanometers to maximize the accessible electrochemical surface area, while maintaining high

proton conductivity and reactant gas diffusivity.¹⁰ To address challenges in product water management, a microporous layer (MPL) is often added between CL and GDL on the cathode side of PEFCs to improve the maximum attainable current density by shifting the onset of severe mass transport losses to higher current densities.^{11–13} Pore sizes in MPL span the range from hundreds of nanometers to a few micrometers, being an order of magnitude smaller than pores in the GDL. However, wide range of feature sizes represents a challenge when attempting to resolve the three-dimensional (3D) geometries with traditional imaging segmentation techniques.

Common techniques for resolving the 3D structure of these porous layers include micro-computed tomography (micro-CT), synchrotron tomography, and focused ion beam scanning electron microscopy (FIB-SEM).^{14–16} However, translating volumetric data into quantitative properties requires accurately classifying each voxel as pore or material, which is an especially difficult task given the complex nature of pore networks.

Figure 1 displays three popular strategies for segmenting pore structures from tomographic data. Manual annotation is often used for simpler examples. In this case, 3D visual clues are employed to distinguish the different classes. AI can be employed to train a model based on manual annotations. The disadvantage of this method is the difficulty in asserting by eye a correct classification of the pores, resulting in a highly biased and time-consuming result.^{17,18} On the other hand, Otsu thresholding is the most popular method for the segmentation of this type of tomographic volume. Often, a median filter is applied to the volume to smooth the images and reduce possible noise, and then the Otsu algorithm is applied to differentiate between the pores and the materials. The Otsu algorithm is a

*Electrochemical Society Member.

^zE-mail: a.colliard@fz-juelich.de; m.eslamibidgoli@fz-juelich.de

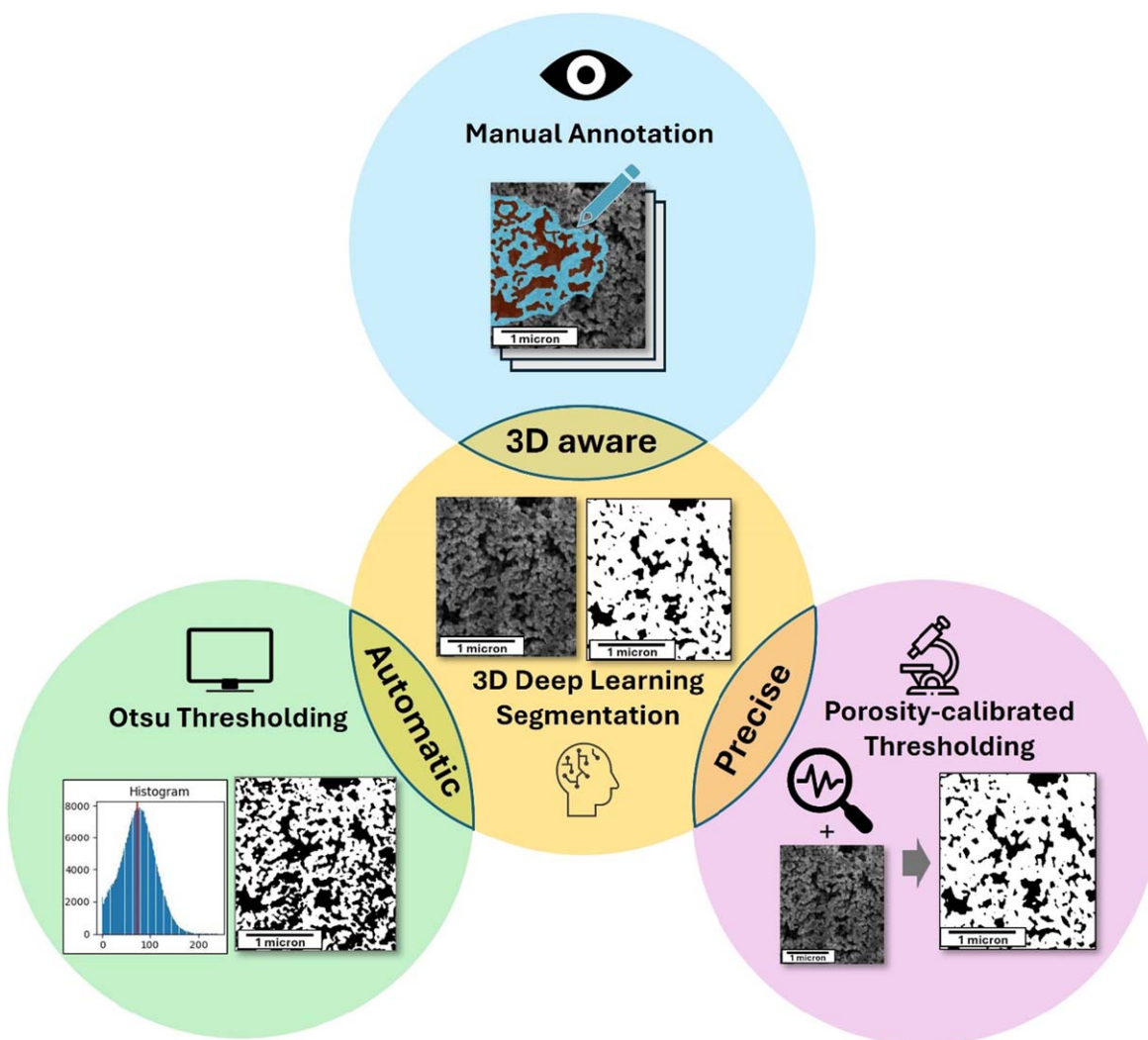


Figure 1. A schematic comparison of available methodologies for pore segmentation is presented on the example of catalyst layers. Standard methods offer distinct advantages: manual annotation benefits from 3D spatial awareness, Otsu thresholding is a fast and fully automated technique, and thresholding based on porosity measurements delivers precise segmentation. In contrast, 3D deep learning-based segmentation combines these advantages into a single method.

binarization algorithm that automatically finds the optimal threshold value by minimizing the intra-class variance between the black and white pixels. The disadvantage of this method is the lack of control over the output, which is solely based on the mathematical separation of the grayscale histogram, rather than corresponding to the real material structure.^{19,20} Finally, porosity-calibrated thresholding is also widely used by experimentalists, and it introduces the employment of a physical characteristic of the sample of interest to tailor the thresholding toward a plausible output. For this calibration, the porosity of the sample must be measured externally, and then the threshold is adjusted to match the measured properties. The main issue of this technique is the need for an extra step with suitable equipment to measure the physical porosity, with an extra complexity layer of different methods yielding different results.^{21,22} Furthermore, all three methods are limited to binary segmentation (i.e., solid vs pore), preventing the distinction of additional layers such as the microporous layer (MPL) from the GDL.

Deep learning (DL)-based image analysis has gained increasing attention in research on PEM-based devices in recent years. Several studies demonstrated the utilization of DL to automate the characterization, ranging from the automation of particle size distribution analysis of catalyst nanoparticles from TEM images, to oxygen bubble dynamics elucidation from optical videos of flow fields, or direct permeability calculation from 3D tomographs of gas diffusion layers.^{23–26}

Algorithms such as DL and computer vision (CV) also emerge as an effective alternative for automating annotation, segmentation, and analysis tasks in binary and multiclass settings for accelerating imaging analysis on energy materials.^{27–29} As depicted in Fig. 1, the employment of 3D DL models combines the best characteristics of each method; it enables the automatic segmentation of volumes, it is aware of the 3D nature of the structures, and it has the precision learned from porosity-calibrated datasets. DL is especially efficient in cases of large volumes of imaging data where the time-consuming nature of manual analyses represents significant bottlenecks.^{30,31} Although DL and CV techniques can automate feature extraction across various domains, the diversity of research fields and the distinct characteristics of their imaging data such as differences in resolution, contrast, noise levels or employed equipment often necessitate the development of tailored AI models that incorporate specialized network architectures alongside domain-specific preprocessing and post-processing steps to effectively address each field's unique tasks.^{23,24,32}

For the specific task of segmenting GDLs, CLs, and MPLs, multiple studies have explored both conventional and machine learning-based approaches. Pfrang et al. approached the task conventionally by applying diffusion filtering and grayscale thresholding to separate GDL and MPL and analyze MPL thickness at the microscale.³³ Nevertheless, conventional image processing methods and grayscale-based algorithms struggle when pixel intensities lack a

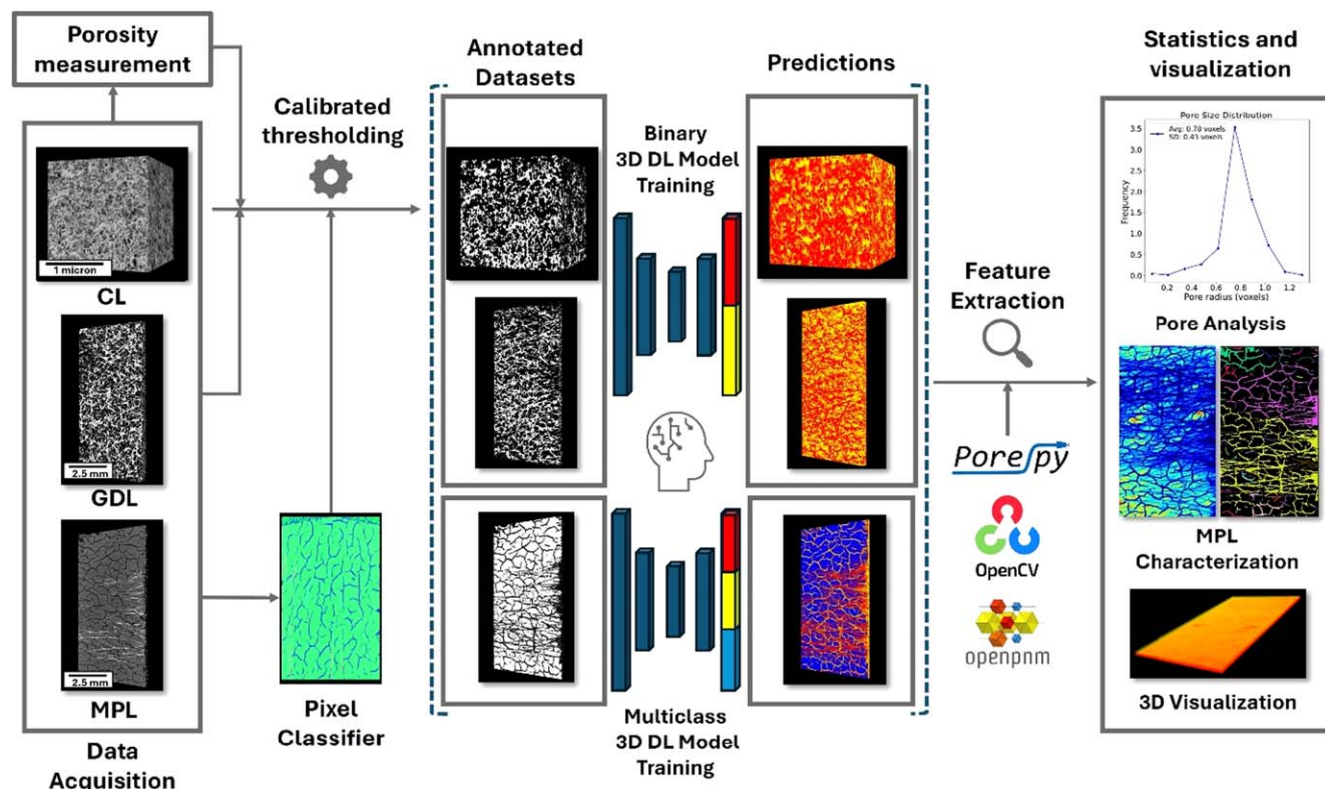


Figure 2. Methodological pipeline for the porous media analysis of CLs, GDLs, and MPLs from 3D micro-CT and electron microscopy-based tomographies.

clear bimodal distribution or exhibit gradual intensity gradients. By employing DL, Mohidivara et al. compared two- and three-dimensional U-Net architectures against manual and semi-automatic annotation procedures for multiclass segmentation in wet GDL tomographies.¹⁸

Shum et al. investigated multiclass machine learning-based segmentation and basic image processing algorithms for water segmentation in GDLs. Their results highlighted that a limited dataset size can hinder the full potential of AI-based methods, emphasizing the need for large, well-annotated training sets.³⁴ However, while supervised machine learning approaches are advantageous in integrating pixel intensity with structural features, they often encounter the challenge of annotating complex porous structures, which can be both time-consuming and prone to user subjectivity. Moreover, synthetic datasets have been employed to train deep learning models for separating GDL fibers from binder, streamlining data acquisition, but potentially compromising realism by introducing uncertainty when the models are applied to real images.³⁵

Recent advances in the field of 3D electron- and X-ray tomography for porous carbon supports in fuel cell electrodes have yielded fruitful methodologies for the analysis of porous materials in similar use cases. Yang et al. developed a sparse-section, U-Net-based pipeline for electron-tomography reconstructions of porous carbon supports in catalyst layers of PEFCs, achieving sub-10 nm segmentation accuracy and cutting manual tuning by over 80%.³⁶ In another work, Yang et al. applied a DL morphological-distribution framework to combine electron- and X-ray-tomography stacks of metal-alloy catalysts, enabling rapid extraction of multi-scale pore metrics in under a minute per volume.³⁷ In the same field, Hong et al. applied automated segmentation to FIB-SEM/ET stacks of aged carbon supports, quantitatively mapping nanoscale pore network degradation during PEMFC cycling.³⁸

Building on these advances in learned, multi-scale pore segmentation, we now introduce UTILE-Pore, a 3D deep learning framework that leverages porosity-calibrated masks to deliver rapid,

accurate binary and multiclass segmentation of FIB-SEM and micro-CT volumes across CL, MPL, and GDL layers. The resulting pipeline reduces the time required for analyzing 3D volumes of porous media and performing porosity measurements to mere seconds, while enabling the segmentation of additional classes. Moreover, users can easily replace the pre-trained models with their own custom models, broadening the framework's applicability.

Experimental

Figure 2 illustrates the workflow developed in this work for autonomously analyzing porous structures in CLs and GDLs with and without MPL. The process begins with data acquisition to generate a robust dataset for training DL models. In total, 33 samples comprising various CLs and GDL samples from commercially available PEFC and PEWE components were collected. The dataset for model training was compiled through the acquisition of volumetric data from FIB-SEM of CLs and micro-CT measurements of GDLs with and without an MPL. Our primary goal is to characterize the porous architecture of CL and GDL, by distinguishing between pore and material phases. For the GDL, a further distinction between fibers and PTFE binder from the collected datasets is not feasible due to nearly identical X-ray attenuation, and sub-micron PTFE coatings fall below our voxel size and cannot be reliably resolved. Furthermore, although the MPL is itself a porous medium, its pore sizes lie below the $\approx 3 \mu\text{m}$ voxel resolution limit of micro-CT scans. Consequently, resolving both GDL and MPL pores simultaneously with micro-CT is not feasible. To maintain accuracy, we therefore treat the MPL as a homogeneous solid and instead focus on macroscale MPL descriptors: crack density, layer thickness, and intrusion depth into the GDL, using the same imaging data. Due to the similarities between MPL and CL the same algorithms could be used on FIB-SEM data for the MPL in future work.

FIB-SEM measurements on CLs were recorded following a consistent FIB-SEM protocol. For the FIB-SEM procedure, a Zeiss Crossbeam 350 with Atlas Engine for 3D Tomography was used.

The single-sided catalyst-coated membrane was glued with the cathode facing up using conductive carbon pads, while the catalyst layer was connected with silver glue to the SEM stub. FIB tomography was carried out at 54° sample tilt (−36° image correction applied) and at a working distance of 5.1 mm (coincidence point of electron and gallium beam). All FIB operation was performed at a voltage of 30 kV. Before starting the tomography, the gas injection system (Platinum and Carbon) was used to deposit a platinum protective layer with the FIB beam at 700 pA, followed by milling of tracking marks at 100 pA with the FIB beam. Finally, these tracking marks were filled with carbon, and an additional carbon layer was deposited on top to protect these structures. These preparation steps were followed by milling the coarse trench with a 7 nA FIB beam and milling the fine trench with a 1.5 nA FIB beam. Secondary electron (E-T) and material contrast (ESB) detectors were used for grabbing the slice images with a thickness of 10 nm per slice and 10 nm pixel size, resulting in 10 nm³ voxels. The milling beam was chosen to be 700 pA at 30 kV. Drift compensation, auto contrast, and auto stigmastism correction were activated during the run. A total of 1508 slices were taken and interpolated to exactly 10 nm per slice with Zeiss Atlas software.

Meanwhile, micro-CT measurements for both plain and micro-porous-layer-containing GDLs were acquired employing a ProCon X-ray CT-MINI (ProCon X-ray GmbH, Sarstedt, Germany) using an X-ray source voltage and current of 30 keV and 200 μ A, respectively, at a working distance of 38.11 mm, resulting in a voxel resolution of 5 μ m. A total of 2000 radiographic projections were acquired over a 360° stage rotation, and later reconstructed using VGSTUDIO MAX (Volume Graphics GmbH, Heidelberg, Germany).

Each dataset was a reconstructed multipage TIFF file, only containing relevant slices with an average height and width of 1000 pixels. The depth of the datasets was highly dependent on the sample, having an average of 40 to 60 slices for the GDL examples and an average of 700 slices for the CL examples.

To generate the training masks for binary segmentation, first, the physical porosity was measured for each sample. Mercury intrusion porosimetry was employed for the porosity measurement of CL datasets, while a pycnometer was used for the GDL micro-CT datasets. For GDLs containing MPL, additional steps were required: First, a pixel classifier (Labkit-Tool in ImageJ)^{39,40} semi-automatically segmented the MPL; second, the MPL voxels were isolated and removed from the volume, leaving only fibers and pores to be calibrated against the measured porosity. Finally, the removed MPL voxels were reintroduced into the volume, resulting in three distinct categories: MPL, fibers, and pores. The physical porosity used to calibrate each segmentation threshold has an absolute repeatability of ± 2 percentage points for Mercury intrusion porosimetry (CL samples) and ± 0.5 percentage points for gas-pycnometry (GDL samples). Because the threshold shifts by only the instrument's error band, only voxels very close to the pore–solids interface can flip labels, a fraction too small (<2%) to affect overall training or performance ranking. Consequently, we train all models on the nominal masks without additional threshold jitter.

The next step is the preprocessing of the volumetric data to prepare it for the model training. Since the tomographic datasets varied in size and 3D models are computationally expensive, each volume was divided into $96 \times 96 \times 96$ voxel cubes. Any cube at the periphery that could not fulfill the standard size was expanded via mirroring to fill the missing regions. A total of 3666 cubes were generated for the binary case and 847 for the ternary case.

To handle the binary and the multiclass tasks, we developed two distinct models. The first binary model is utilized for segmenting GDLs and CLs, whereas a multiclass model is used to distinguish GDL fibers, pores, and MPL. For both cases, we benchmarked a selection of three well-established 3D architectures from the literature to identify the most effective one for each case: 3D UNet with a ResNeXt101 backbone, 3D VNet, and 3D Swin UNet, with the calibrated masks serving as ground truth.

–**3D UNet with a ResNeXt101 backbone** combines the fully convolutional 3D UNet encoder–decoder structure with the ResNeXt101 backbone for feature extraction. The standard 3D UNet employs skip connections to merge low- and high-resolution features, improving boundary delineation. ResNeXt101 integrates a split-transform-merge strategy, referred to as “cardinality,” which provides multiple parallel paths within each block without increasing network depth or width. Incorporating ResNeXt101 into the 3D UNet thus enables more efficient capture of complex spatial patterns.^{41,42}

–**3D VNet** architecture retains the UNet encoder–decoder framework with skip connections but replaces standard convolutional layers with residual blocks. These residual connections aim to expedite convergence and enhance segmentation accuracy, particularly for volumetric data where continuity along the depth dimension is crucial. In addition, this design may require fewer training samples than non-residual counterparts.⁴³

–**3D Swin UNet** combines the UNet encoder–decoder layout with Swin transformers, which employ window-based self-attention to effectively capture both local and global dependencies. Unlike convolution-based networks, which rely on fixed receptive fields, Swin transformers dynamically adjust receptive fields based on dataset requirements. This flexibility enables more robust modeling of long-range spatial relationships in 3D volumes.⁴⁴

During the training phase, the primary objective was to minimize the loss function, which quantifies the discrepancy between the predictions and the porosity-calibrated ground truth. The 3666 binary samples and the 874 ternary samples were split into an 80:20 ratio for training and validation. Each complete pass through the training dataset, called an epoch, refines the model's parameters based on the computed loss. Each model was trained over 100 epochs with a batch size of 4, using the Adam optimizer and binary or categorical cross-entropy as the loss function. Convergence occurs once the loss reaches a minimum, guided by an appropriately tuned learning rate. The learning rate was dynamically reduced from 10^{-4} to 10^{-6} once the loss reached a plateau, but constrained to avoid dropping to negligible values. After each epoch, the model's performance was assessed on the unseen validation set to evaluate its robustness and generalization ability. To improve the positional robustness of the models, we augmented the employed data with on-the-fly random flips in the x, y, and z directions. Furthermore, the memory-demanding 3D model training with a batch size of 4 was parallelized on 4 Nvidia GPUs V100 with mixed precision protocols. Additional scripts and the employed datasets are available at the GitHub and Zenodo repositories cited in the data availability statement.

After the training phase, we systematically evaluated the performance of each model using standard metrics. We compared the predicted classification of each voxel against the ground truth, assigning it to one of four categories: true positive (TP) for voxels correctly identified as positive, false positive (FP) for voxels incorrectly classified as positive, true negative (TN) for voxels correctly recognized as negative, and false negative (FN) for voxels misclassified as negative when they were actually positive. By combining these counts, we calculated precision (Eq. 1), recall (Eq. 2), and F1-score (Eq. 3) to achieve a comprehensive view of model performance. Precision measures how accurate the positive predictions are, while recall quantifies the proportion of actual positives that were successfully identified. The F1-score, defined as the harmonic mean of precision and recall, balances these two metrics to provide an overall measure of model accuracy.

$$\text{Precision} = \frac{TP}{TP + FP}; \quad [1]$$

$$\text{Recall} = \frac{TP}{TP + FN}; \quad [2]$$

$$F1 = 2 \times \text{Precision} \times \frac{\text{Recall}}{\text{Precision} + \text{Recall}}. \quad [3]$$

Once the model was trained, to predict new examples, the input volumes also need to be cropped into cubes of $96 \times 96 \times 96$ voxels. The cubes are then predicted by the model, and subsequently the cubes need to be repatched back to the original shape. To ensure a smooth transition between the patches, the cubes are cropped with a certain overlap, and by repatching, we employ a Gaussian weight to blend the predictions.

After generating the segmentation volumes from the input data, we developed specialized computer vision and mathematical functions to perform additional analyses and extract quantitative information. These analyses are grouped into two categories: (1) functions for binary segmentations (i.e., GDL and CL), and (2) functions for multiclass segmentations (i.e., the interplay between MPL and GDL).

For the binary segmentations, we introduced methods to measure porosity and surface roughness, and we integrated PoreSpy⁴⁵ for pore size distribution analysis and tortuosity simulation, which can be computationally intensive but benefits from GPU acceleration. Estimating permeability is more complex and typically requires manual parameter adjustments; thus, our tool employs the Kozeny–Carman equation (Eq. 4) as an approximation.⁴⁶ This equation describes the pressure drop of fluid flow through a packed bed of solids and is expressed as:

$$k = \frac{\varepsilon^3}{C\tau^2(1 - \varepsilon)^2(S_v)^2}, \quad [4]$$

Where ε denotes the porosity, τ the tortuosity, S_v the specific surface area, and C the Kozeny constant. The Kozeny–Carman equation allows for a permeability estimate by incorporating porosity and tortuosity values extracted from our predictive models. The Kozeny constant C , typically ranging from 4 to 5, encapsulates geometric factors, including pore packing and particle shape. The specific surface area is derived by converting the segmented structure into a mesh and measuring the polygonal surface areas.

Because the Kozeny–Carman equation provides only an approximation, and our goal is to support more advanced simulations, we included the functionality to export the segmented volumes directly into PoreSpy and OpenPNM⁴⁷ formats for further analyses.

The surface roughness is calculated by cropping the upper layers of the binary volume, converting them into a mesh, and measuring depth variations at each vertex to quantify roughness across the entire structure.

For the MPL–GDL configurations, we created functions to analyze MPL cracks, map variations in MPL thickness, quantify the extent of MPL intrusion into the GDL, and calculate the surface areas of both the MPL and GDL.

Specifically, for the MPL intrusion quantification, we employed the advantages of having a precise segmentation of the bulk MPL and the power of CV to measure the variations of thickness through the layer. For this reason, we first measured the total roughness of the MPL facing the GDL. Subsequently, we divided the MPL into smaller regions and calculated the local roughness of each patch. The standard deviation of the local roughness gave an insight into

the depth variation of the MPL through the layer. Additionally, we calculated the dimensionless coefficient of variation c_{R_a} (Eq. 5) for comparability purposes, given by

$$c_{R_a} = \frac{\sigma_{R_a}}{R_a}, \quad [5]$$

With c_{R_a} representing the relative variability of the roughness, σ_{R_a} being the standard deviation of the surface roughness, and R_a the total roughness.

All derived measurements are automatically visualized in 3D using the Visualization Toolkit (VTK)⁴⁸ library, enabling interactive exploration of the predicted volumes. The software also supports generating short GIFs of the rotating 3D volumes, enhancing the ease of communication and presentation of the results.

Results and Discussion

Table I compares performance metrics for all binary models, with results indicating that the models performed similarly over the other architectures based on F1-scores. To further evaluate real-world applicability, an unseen GDL volume with a physically measured porosity of 73.7% was segmented by each model. For a better comparability of the models based on the computed parameters, we added columns to depict the porosity difference Δ_p , the tortuosity difference Δ_τ , and the specific surface area difference Δ_{SSA} , (Eqs. 6a–6c) which are defined as,

$$\Delta_p = |p_{real} - p_{pred}|, \quad [6a]$$

$$\Delta_\tau = |\tau_{real} - \tau_{pred}|, \quad [6b]$$

$$\Delta_{SSA} = |SSA_{real} - SSA_{pred}| \quad [6c]$$

With Δ_x being the positive deviation of the predicted parameter x_{pred} and the parameter derived from the physically calibrated volume x_{real} .

Table I compares three 3D convolutional neural network (CNN) architectures on a binary pore–solid segmentation task. All models achieve similar F1-scores, but the 3D V-Net shows the closest match to physical porosity measurements. Although the 3D U-Net records the highest F1-score, the V-Net yields the smallest absolute porosity error ($\Delta_p = 1.7\%$), roughly half the U-Net's 3.9%. Here, Δ_p denotes the absolute difference between measured and predicted porosity, and values below the pycnometer's $\pm 0.5\%$ repeatability lie within calibration noise. The V-Net's superior performance stems from its volumetric residual blocks and symmetric encoder–decoder structure, which preserve fine boundary details and sharpen the fiber–void interface. Its larger effective receptive field and dense skip connections reduce over-segmentation of narrow throats without compromising tortuosity deviation (0.44%) or specific surface area deviation ($0.78 \mu\text{m}^{-1} \cdot 10^{-2}$).

This improved porosity fidelity leads to visibly sharper segmentations in Fig. 3. In the catalyst-layer (CL) scenario, all networks reconstruct the overall pore network, but the V-Net maintains the finest solid–void boundaries and preserves thin material regions near

Table I. Comparison of different 3D deep learning architectures trained on a unique binary dataset of CLs and GDLs. The performance of the models is assessed by employing the standard metrics of precision, recall, and F1-score, and additionally by the porosity difference Δ_p , the tortuosity difference Δ_τ , and the specific surface area difference Δ_{SSA} .

Model	Precision [%]	Recall [%]	F1-Score [%]	Δ_p [%]	Δ_τ	$\Delta_{SSA} [\mu\text{m}^{-1} \cdot 10^{-2}]$
3D VNet	91	89	90	1.7	0.44	0.78
3D UNet	89	91	91	3.9	0.03	0.52
3D SwinUNet	83	88	85	2.4	0.53	0.46
Otsu thresholding	—	—	—	5	1.14	0.44

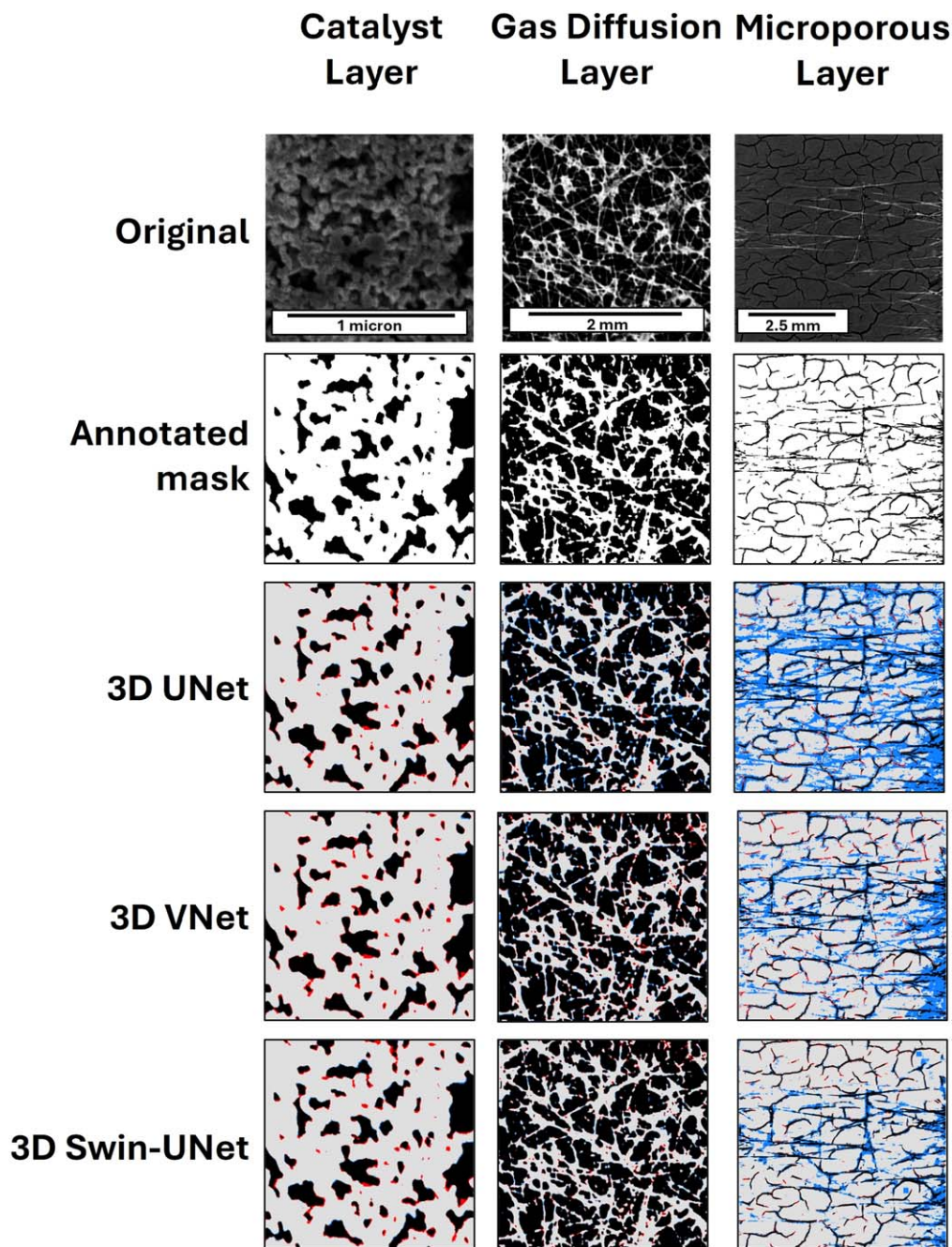


Figure 3. Comparative visualization of the original images with the corresponding annotated mask for the three types of datasets in consideration in this work: CLs, GDLs, and GDLs with MPLs. Gray pixels indicate true positives for correctly detected material, blue pixels represent false negatives where material pixels are missed, and red pixels signify false positives for erroneously detected non-material pixels.

the edges. The U-Net delivers comparable bulk segmentation, whereas the Swin U-Net's windowed attention sometimes fractures the smallest CL pores. In the gas diffusion layer (GDL) case, each model captures the high-porosity texture so uniformly that visual assessment alone is insufficient; instead, quantitative metrics drive the evaluation. Overall, the 3D V-Net provides the best combination of segmentation accuracy and transport-property fidelity for binary pore–solid applications.

o4-mini-high.—To benchmark the method against standard laboratory practices, we also compared predicted porosity to the physical measurement and the porosity derived from Otsu thresholding. The Otsu-based approach yielded a Δ_p of 5%, deviating the most from the physical value compared to the evaluated models, and

a tortuosity deviation over twice that of the CNNs ($\Delta_\tau = 1.14\%$), even though the SSA error may appear low. Thus, demonstrating that the model-based prediction was more accurate in the delineation of the fibers in a 3D fashion.

Table II presents the multiclass segmentation results on GDLs containing MPL. The models were trained using 847 cubes of size $96 \times 96 \times 96$ voxels extracted from 10 tomographs of commercially available GDLs with MPL, employing the same training parameters as before. The metrics indicate a high similarity in the performance of the diverse models. To validate the highest performing architecture, we compared the predicted porosity of the GDL (excluding the MPL) with the physically measured porosity for a sample without MPL. The 3D SwinUNet achieves the smallest porosity error of Δ_p of 3.3%, despite having a lower overall F1. We hypothesize that its

Table II. Comparison of different 3D deep learning architectures trained on a unique ternary multiclass dataset of CLs, GDLs, and MPLs. The performance of the models is assessed by employing the standard metrics of precision, recall, and F1-score, and additionally by Δ_p , which is the positive difference between the predicted porosity and the physically measured porosity.

Model	Precision [%]	Recall [%]	F1-Score [%]	Δ_p [%]
3D VNet	83	92	88	9.8
3D UNet	88	90	89	8.4
3D SwinUNet	85	90	88	3.3

windowed self-attention mechanism excels at distinguishing the thin MPL cracks and the subtle grey-level differences at the MPL/GDL interface, features that can be easily lumped together as “solid” by pure convolutional models. By capturing long-range correlations across the volume, SwinUNet more accurately segments these multiclass boundaries, giving it the edge in porosity fidelity for three-phase samples. This is confirmed in Fig. 3, where SwinUNet most faithfully segments the fine MPL cracks and cleanly separates the two layers; by contrast, VNet tends to smooth narrow fissures at the interface, and UNet mislabels small MPL regions as GDL material, slightly blurring the layer boundary.

The implementation of an automatic tomographic volume segmentation approach based on porosity-calibrated volumes combines the precision of the thresholding approach based on real physical information from the sample with the advanced 3D pattern recognition capabilities of 3D deep learning architectures. The model is trained to analyze the three-dimensional context of the materials and precisely delineate the contours of the pores based on the physical properties of the sample. This approach not only removes the need to calculate the physical porosity of each analyzed volume but also enhances the segmentation on complex cases where thresholding may fail.

Furthermore, we developed a unified software that enables experimentalists to quantify structural properties in all scenarios using computer vision algorithms. In Fig. 4, we showcase the implemented functions for binary segmentation, such as an algorithm to count pore and material voxels slice by slice and thereby estimate the sample’s porosity from the model’s predictions, enabling the porosity profile plots. We further integrated functions from the PoreSpy library to characterize pore sizes and generate pore size distribution plots, offering insights into the pore structure of each tomograph. These findings improve material-specific understanding and aim to help experimentalists correlate the structures with other present phenomena, such as wettability or water retention.

The CL presents a clear bias in the porosity profile towards the membrane with a more homogenous porosity towards the bulk of the structure, where we see a sharp increase in porosity from 50%–65% within the first 100 slices of the CL, followed by a consistent 65% porosity thereafter. Again, this porosity inhomogeneity is confirmed by the pore size distribution plot, which shows one main peak, but over a wider range of voxel radii with a minor modal bias. The left-skewed bias indicates the presence of an appreciable number of smaller pores at 4.84 voxels with a standard deviation of 3.20 voxels. The main peak is broad, indicating a wide range of pore sizes with a significant number of smaller pores, particularly concentrated near the low-porosity membrane side. Similarly, our predicted porosity analyses show strong resemblance to CLs reported in the literature. Berejnov et al. leveraged Scanning Transmission X-ray Microscopy (STXM) on PEFC CLs and demonstrated strong porosity gradients between the membrane and the surface of the CL, revealing a low porosity at the membrane interface caused by an abundance of ionomer.⁴⁹ The bimodal pore size distributions further confirm the validity of our technique, and have been both experimentally observed and used for stochastic generation of CLs.^{50,51}

In the case of GDLs, we observe in the porosity profile a certain homogeneity in the porosity through the slices, around 62%–76%, while the pore size distribution analysis confirms the regular pore distribution by showcasing a predominantly single normal bell at pore sizes of 5–6 voxels with a standard distribution of 2.01 voxels. Our predicted porosity profiles and pore size distributions align well with what has been previously reported in the literature. Ince et al. utilized X-ray tomography and revealed GDL porosity profiles above 70% and further revealed local porosity valleys, often towards the centre of the substrate, revealing binder and PTFE agglomerations.⁵² Furthermore, our predicted pore scale distribution, mostly encompassing pore sizes between 25–30 μm , are typical of commercial carbon paper-based GDL.⁵³

In the combined GDL/MPL volume, the slice-by-slice porosity profile reveals three distinct regimes. In the first ~ 10 slices (pure MPL), porosity remains very low (20%–25%), reflecting the dense crack-limited architecture of the MPL. Between slices 10–20, the MPL/GDL interface porosity rises sharply from 25% up to 90% as MPL cracks penetrate into the substrate. Beyond slice 20 (bulk GDL) the porosity then settles into a plateau around 80%–85%, matching the values seen in the GDL-only case. The pore size distribution reveals a broader, bimodal-like pattern with a mean radius of 8.96 voxels (SD: 3.59 voxels). The right-skewed distribution reflects the superposition of two characteristic length scales: larger pores associated with MPL cracks and finer channels from the underlying GDL fiber matrix. Together, these features reproduce the multi-scale pore network expected in an MPL-coated GDL, where fine cracks in the MPL facilitate through-plane transport and the underlying GDL provides the coarser diffusion pathways. Such a heterogeneous, bimodal pore architecture has been correlated with enhanced gas-diffusion performance in MPL-modified GDLs in prior experimental studies.^{54,55}

For the multiclass segmentation model that includes the MPL, we concentrated on characterizing the added layer and its interdependency within the GDL substrate. Additionally, we isolated the MPL region from the segmented volume and performed a direct crack analysis of its surface. We began by extracting the first layer on the MPL side, then employed computer vision algorithms to identify and measure the isolated cracks. This process yielded the total crack area, the distribution of individual crack areas, and a visual representation of these cracks, as illustrated in Fig. 5. In the presented example, the distribution is plotted on a logarithmic scale to showcase the distribution of the crack size in a visually more comprehensive fashion. From the diagram, we can confirm the visual assessment of a small number of large, interconnected cracks and a higher number of smaller cracks through the MPL. The total crack count can be computed at 483, and the cracks represent 25% of the total surface of the MPL. Understanding such cracking behavior can inform strategies for optimizing layer design and improving overall cell performance. For instance, MPLs with cracks have been shown to influence liquid water transport under high humidity conditions, helping to direct excessive water away from the CL.^{56,57} However, despite the minor mass transport improvements, MPL cracks have more recently been linked with platinum migration and raise concerns relating to long-term durability.⁵⁸

We also quantified the extent to which the MPL intrudes into the GDL substrate. First, we measured the average thickness of both layers to contextualize their dimensional scales. To visualize MPL thickness variation across the volume, we generated density maps of the MPL layer (Fig. 5c), along with a 3D rendering, revealing how the MPL distribution changes spatially. For further understanding of the local high-intrusion zones, a function to represent the cross-sectional view of the MPL/GDL interface was included. To go beyond visualization, we then developed a method to quantify the degree of MPL intrusion into the GDL by focusing on the surface roughness of the MPL side in contact with the GDL. Specifically, we calculated the global roughness of this interface, characterized by the standard deviation of height measurements, and expressed it as a coefficient of variation, defined as the ratio of the standard deviation

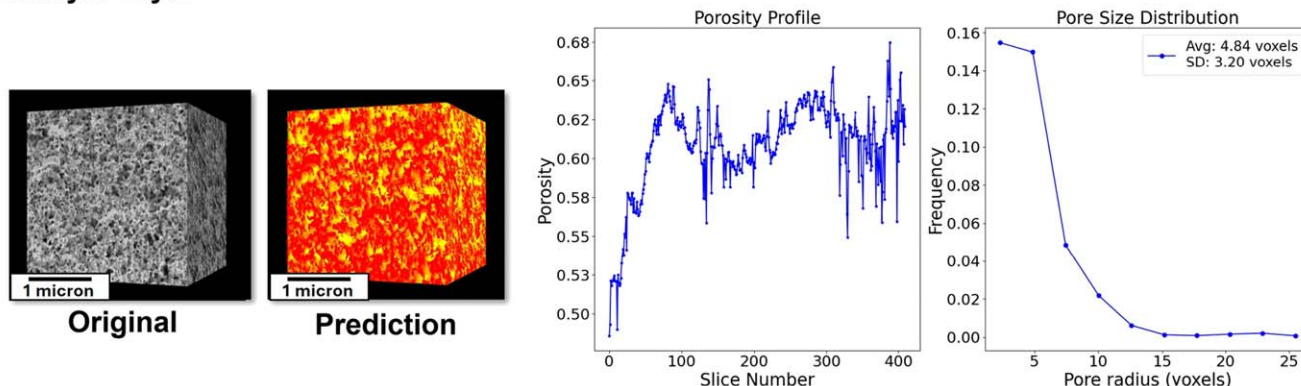
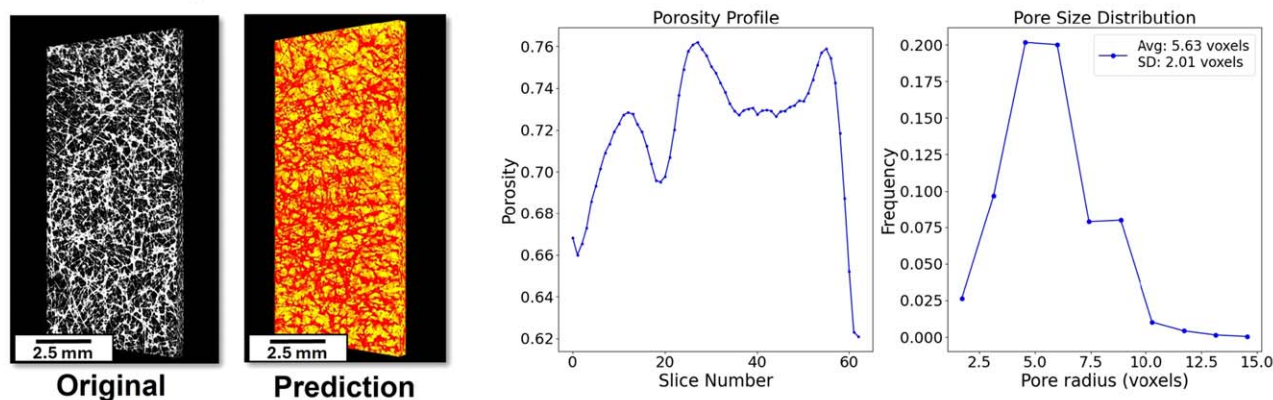
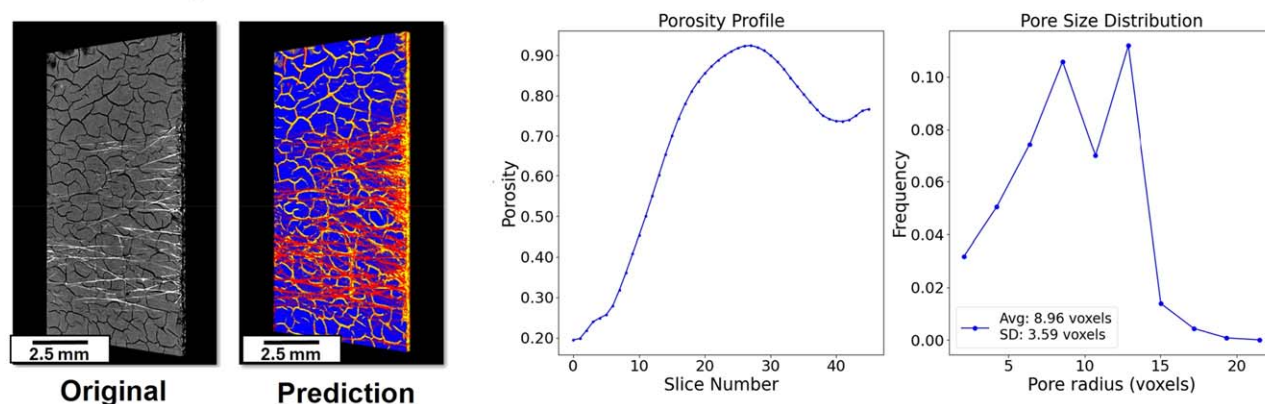
Catalyst Layer**Gas Diffusion Layer****Gas Diffusion Layer + MPL**

Figure 4. Showcase of the property extraction capabilities of the presented tool on CL, GDL, and GDL with MPL segmented volumes. For the segmented tomographies, the tool allows the users to extract pore size distribution analysis, porosity, permeability, and tortuosity simulations.

to the mean roughness value. This provides a quantitative measure of how deeply the MPL intrudes into the GDL.

In this example, we observe in the density map two highly intruded regions toward the middle of the MPL. In the 3D reconstruction, it is possible to observe both intrusions and a certain homogeneity in the rest of the MPL with slight increases in the intrusion towards the top and bottom parts. The maximum MPL thickness of 30 voxels and the average thickness of 6 voxels indicate that the intrusions achieved a high intrusion on the red-hued areas. Since the areas are relatively small in comparison to the rest of the MPL, we observe a small intrusion coefficient of 10%. Accurate quantification of MPL intrusion is critical when optimizing for the next generation of GDL materials. Specifically, the MPL intrusion dictates the degree of diffusion scale overlap and can be tailored to result in a more continuous in-plane pore-scale distribution. These features are both key parameters for developing PEFC and PEWE

sub-component models and achieving desirable in-plane porosity gradients, respectively.^{59,60}

By applying deep learning to MPL-coated GDLs, we derive advanced metrics that were previously inaccessible. Beyond the functions described above, we further calculated the interface area between the MPL and the GDL. Specifically, we examined the neighbors of each MPL voxel and counted those that were adjacent to a GDL voxel. This surface area metric provides an additional quantitative measure of MPL intrusion into the GDL.

Conclusions

UTILE-Pore is an integrated 3D deep-learning pipeline that combines porosity-calibrated ground-truth masks with cutting-edge volumetric convolutional neural networks and transformer models to automate the segmentation of FIB-SEM and micro-CT tomograms.

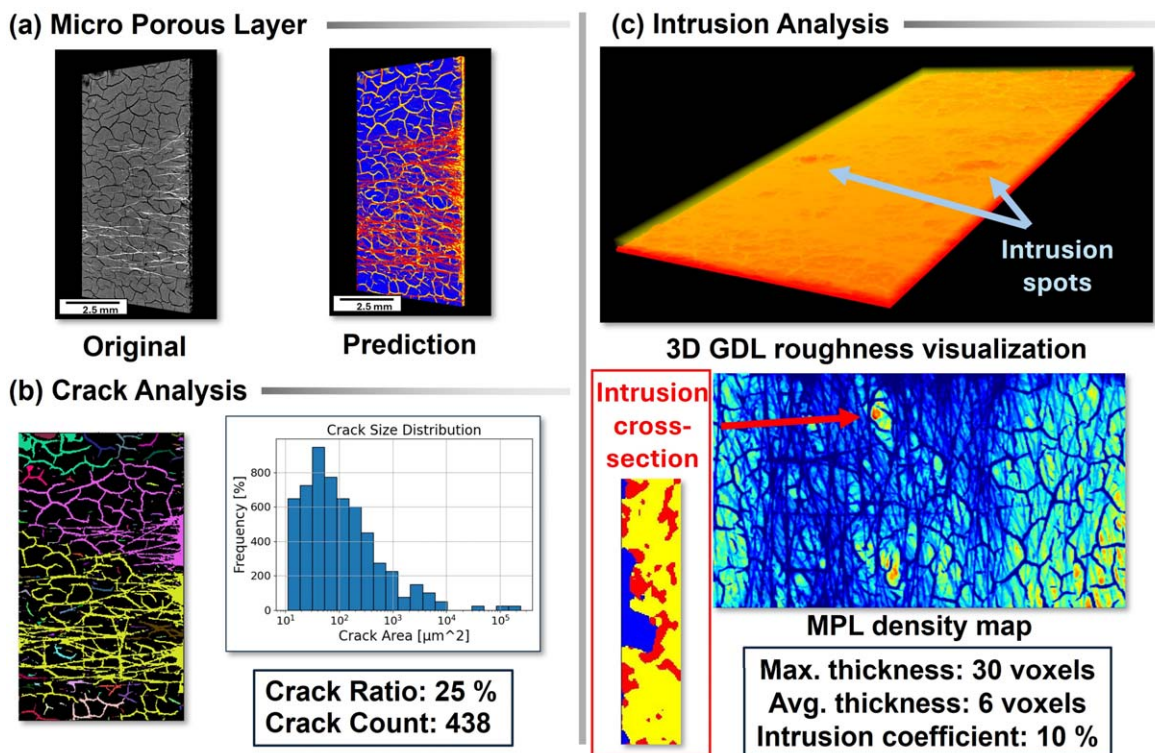


Figure 5. (a) Visual comparison of the original GDL with MPL volume and the obtained multiclass segmentation. (b) Example of crack analysis and visualization capabilities of the software, showcasing the segmented MPL. (c) Visualizations of the intrusion analysis of the MPL into the GDL substrate. To support the intrusion analysis, the software presents a 2-dimensional visualization of the intruded MPL as a density map and as a cross-sectional view. It computes a 3D interactive visualization for further inspection of the regions of interest. The intrusion is quantified based on local roughness analysis and its deviation from the normal distribution. Additionally, our software computes the maximum and average thickness of the MPL.

It focuses on CL, GDL, and MPL, replacing the time-consuming manual annotation and *ad hoc* thresholding by incorporating physical porosity measurements during model training. This approach enables both reliable binary (CL/GDL) and multiclass (MPL, GDL, and pores) segmentation within a single platform.

In seconds, UTILE-Pore generates binary and multiclass segmentations and immediately extracts vital structural and transportation properties, such as pore-size distributions, porosity, tortuosity, specific surface area, and permeability estimates via the Kozeny–Carman equation. For MPL-coated GDLs, it also assesses interlayer characteristics, such as crack density, crack size distributions, MPL thickness, and intrusion depth, using connected-component and roughness analyses. Interactive 3D visualizations and quantitative plots enable rapid correlation between microstructure and performance metrics, while automated export to PoreSpy/OpenPNM formats facilitates subsequent theoretical modeling.

To achieve a comprehensive multiscale characterization, we intend to integrate higher-resolution and phase-contrast imaging modalities (e.g., nano-CT, hierarchical CT, advanced FIB-SEM, and synchrotron tomography) in the future to allow for direct 3D segmentation of sub-micron MPL pores and PTFE binder distributions. We plan to release UTILE-Pore as a modular design publicly, encouraging the community to integrate extra computer-vision tools, larger neural network architectures, and enhanced visualization capabilities, which will promote widespread usage and ongoing improvements in polymer-electrolyte-membrane devices.⁶¹

Acknowledgments

The authors acknowledge the financial support from the Helmholtz Imaging HI (a platform of the Helmholtz Incubator on Information and Data Science) grant number DB002249, as well as the Federal Ministry of Science and Education (BMBF) under the German-Canadian Materials Acceleration Centre (GC-MAC) grant

number 01DM21001A. The authors ACG, KM, MHE, and MJE also acknowledge the partial financial support from the European Union's Horizon Europe Research and Innovation programme, project DECODE under Grant Agreement No. 101135537. The authors also acknowledge the Gauss Centre for Supercomputing e.V. (<https://www.gauss-centre.eu>) for funding this project by providing computing time on the GCS Supercomputer JUWELS at Jülich Supercomputing Centre (JSC) of Forschungszentrum Jülich. The research leading to the results received funding from the Fuel Cells and Hydrogen 2 Joint Undertaking (now Clean Hydrogen Partnership) under Grant Agreement No 875025 (Further-FC). This Joint Undertaking receives support from the European Union's Horizon 2020 Research and Innovation program, Hydrogen Europe and Hydrogen Europe Research. The authors also want to thank Martina Gerle, DLR for performing MIP measurement of the catalyst layer. The authors acknowledge the use of ChatGPT (OpenAI) and DeepL Write for grammar and style editing of text originally drafted by the authors. All intellectual and conceptual content was solely provided by the authors, who take full responsibility for the integrity and accuracy of the final manuscript.

Authors Contributions










André Colliard-Granero: Conceptualization, data acquisition, methodology, software, visualization, writing—original draft, writing—review & editing. Salvatore Ranieri: conceptualization, writing—original draft, writing—review & editing. Aimy Bazylak: supervision, writing—original draft, writing—review & editing. Jasna Jankovic: data acquisition, supervision, writing—original draft, writing—review & editing. Tobias Morawietz: data acquisition, supervision, writing—original draft, writing—review & editing. K. Andreas Friedrich: supervision, writing—review & editing. Michael H. Eikerling: conceptualization, supervision, writing—original draft, writing—review & editing. Kourosh

Malek: conceptualization, supervision, writing—original draft, writing—review & editing. Mohammad J. Eslamibidgoli: conceptualization, supervision, visualization, writing—original draft, writing—review & editing.

Data Availability

The code and demonstration of the model predictions can be found in the repository UTILE-Pore at <https://github.com/andyco98/UTILE-Pore>. The employed annotated dataset and the trained model are accessible at Zenodo: <https://doi.org/10.5281/zenodo.15100898>

ORCID

André Colliard-Granero  <https://orcid.org/0000-0002-4615-3710>
Salvatore Ranieri  <https://orcid.org/0009-0003-6874-2465>
Aimy Bazylak  <https://orcid.org/0000-0002-9594-4930>
Tobias Morawietz  <https://orcid.org/0000-0003-2291-9360>
K. Andreas Friedrich  <https://orcid.org/0000-0002-2968-5029>
Jasna Jankovic  <https://orcid.org/0000-0001-8267-9560>
Michael H. Eikerling  <https://orcid.org/0000-0002-0764-8948>
Kourosh Malek  <https://orcid.org/0000-0002-3021-0813>
Mohammad J. Eslamibidgoli  <https://orcid.org/0000-0002-5057-2993>

References

- Y. Guo, G. Li, J. Zhou, and Y. Liu, "Comparison between hydrogen production by alkaline water electrolysis and hydrogen production by PEM electrolysis." *IOP Conf. Ser.: Earth Environ. Sci.*, IOP Publishing, **371**, 042022 (2019).
- I. Sinapan, C. Lin-Kwong-Chon, C. Damour, J.-J. A. Kadjo, and M. Benne, "Oxygen bubble dynamics in PEM water electrolyzers with a deep-learning-based approach." *Hydrogen*, **4**, 556 (2023).
- M. Carmo, D. L. Fritz, J. Mergel, and D. Stolten, "A comprehensive review on PEM water electrolysis." *Int. J. Hydrogen Energy*, **38**, 4901 (2013).
- M. Eikerling, A. A. Kornyshev, and A. A. Kulikovskiy, *Physical modeling of fuel cells and their components* (John Wiley & Sons, Ltd, Encyclopedia of Electrochemistry) (2007).
- M. Eikerling and A. Kulikovskiy, *Polymer Electrolyte Fuel Cells: Physical Principles of Materials and Operation* (CRC Press, USA) (2014).
- E. Wallnöfer-Ogris, I. Grimmer, M. Ranz, M. Höglinger, S. Kartusch, J. Rauh, M.-G. Macherhammer, B. Grabner, and A. Trattner, "A review on understanding and identifying degradation mechanisms in PEM water electrolysis cells: insights for stack application, development, and research." *Int. J. Hydrogen Energy*, **65**, 381 (2024).
- F. A. de Bruijn, V. Dam, and G. Janssen, "Durability and degradation issues of PEM fuel cell components." *Fuel cells*, **8**, 3 (2008).
- H. Xu, M. Bührer, F. Marone, T. J. Schmidt, F. N. Büchi, and J. Eller, "Effects of gas diffusion layer substrates on PEFC water management: Part I. Operando liquid water saturation and gas diffusion properties." *J. Electrochem. Soc.*, **168**, 074505 (2021).
- N. Ge, R. Banerjee, D. Muirhead, J. Lee, H. Liu, P. Shrestha, A. Wong, J. Jankovic, M. Tam, and D. Susac, "Membrane dehydration with increasing current density at high inlet gas relative humidity in polymer electrolyte membrane fuel cells." *J. Power Sources*, **422**, 163 (2019).
- J. Zhao, H. Liu, and X. Li, "Structure, property, and performance of catalyst layers in proton exchange membrane fuel cells." *Electrochemical Energy Reviews*, **6**, 13 (2023).
- Y.-C. Chen, T. Dörenkamp, C. Csoklich, A. Berger, F. Marone, J. Eller, T. J. Schmidt, and F. N. Büchi, "On the water transport mechanism through the microporous layers of operando polymer electrolyte fuel cells probed directly by X-ray tomographic microscopy." *Energy Advances*, **2**, 1447 (2023).
- P. Antonacci, S. Chevalier, J. Lee, N. Ge, J. Hinebaugh, R. Yip, Y. Tabuchi, T. Kotaka, and A. Bazylak, "Balancing mass transport resistance and membrane resistance when tailoring microporous layer thickness for polymer electrolyte membrane fuel cells operating at high current densities." *Electrochim. Acta*, **188**, 888 (2016).
- J. Lee, R. Yip, P. Antonacci, N. Ge, T. Kotaka, Y. Tabuchi, and A. Bazylak, "Synchrotron investigation of microporous layer thickness on liquid water distribution in a PEM fuel cell." *J. Electrochem. Soc.*, **162**, F669 (2015).
- M. Shojaefard, G. Molaeimanesh, M. Nazemian, and M. Moqaddari, "A review on microstructure reconstruction of PEM fuel cells porous electrodes for pore scale simulation." *Int. J. Hydrogen Energy*, **41**, 20276 (2016).
- U. Panchenko, T. Arlt, I. Manke, M. Müller, D. Stolten, and W. Lehnert, "Synchrotron radiography for a proton exchange membrane (PEM) electrolyzer." *Fuel Cells*, **20**, 300 (2020).
- M. Ahmed-Maloum, T. David, L. Guetaz, A. Morin, J. Pauchet, M. Quintard, and M. Prat, "Characterizing PEM fuel cell catalyst layer properties from high resolution three-dimensional digital images, part I: a numerical procedure for the ionomer distribution reconstruction." *Int. J. Hydrogen Energy*, **80**, 39 (2024).
- S. Claes, W. Van De Walle, M. Islahuddin, and H. Janssen, "The application of computed tomography for characterizing the pore structure of building materials." *J. Building Phys.*, **43**, 254 (2020).
- M. Mahdaviara, M. J. Shojaei, J. Siavashi, M. Sharifi, and M. J. Blunt, "Deep learning for multiphase segmentation of X-ray images of gas diffusion layers." *Fuel*, **345**, 128180 (2023).
- K. Abrosimov, K. Gerke, I. Semenov, and D. Korost, "Otsu's algorithm in the segmentation of pore space in soils based on tomographic data." *Eurasian Soil Science*, **54**, 560 (2021).
- I. V. Zenyuk, D. Y. Parkinson, L. G. Connolly, and A. Z. Weber, "Gas-diffusion-layer structural properties under compression via X-ray tomography." *J. Power Sources*, **328**, 364 (2016).
- P. Iassonov, T. Gebrenegus, and M. Tuller, "Segmentation of X-ray computed tomography images of porous materials: A crucial step for characterization and quantitative analysis of pore structures." *Water Resour. Res.*, **45**, W09415 (2009).
- H. Li, T. Qiao, and X. Ding, "Effect of grayscale threshold on X-ray computed tomography reconstruction of gas diffusion layers in polymer electrolyte membrane fuel cells." *Heliyon*, **10**, e29378 (2024).
- A. Colliard-Granero, M. Batool, J. Jankovic, J. Jitsev, M. H. Eikerling, K. Malek, and M. J. Eslamibidgoli, "Deep learning for the automation of particle analysis in catalyst layers for polymer electrolyte fuel cells." *Nanoscale*, **14**, 10 (2022).
- A. Colliard-Granero, K. A. Gompou, C. Rodenbücher, K. Malek, M. Eikerling, and M. J. Eslamibidgoli, "Deep learning-enhanced characterization of bubble dynamics in proton exchange membrane water electrolyzers." *Phys. Chem. Chem. Phys.*, **26**, 14529 (2024).
- A. Colliard-Granero, J. Jitsev, M. H. Eikerling, K. Malek, and M. J. Eslamibidgoli, "UTILE-gen: automated image analysis in nanoscience using synthetic dataset generator and deep learning." *ACS Nanoscience Au*, **3**, 398 (2023).
- T. Cawte and A. Bazylak, "A 3D convolutional neural network accurately predicts the permeability of gas diffusion layer materials directly from image data." *Current Opinion in Electrochemistry*, **35**, 101101 (2022).
- X. Liu, K. Fan, X. Huang, J. Ge, Y. Liu, and H. Kang, "Recent advances in artificial intelligence boosting materials design for electrochemical energy storage." *Chem. Eng. J.*, **490**, 151625 (2024).
- A. Aspuru-Guzik and K. Persson, *Materials Acceleration Platform: Accelerating Advanced Energy Materials Discovery by Integrating High-Throughput Methods and Artificial Intelligence* (Canadian Institute for Advanced Research, Canada) (2018).
- M. Batool, O. Sanumi, and J. Jankovic, "Application of artificial intelligence in the materials science, with a special focus on fuel cells and electrolyzers." *Energy and AI*, **18**, 100424 (2024).
- Z. Deng, X. Lin, Z. Huang, J. Meng, Y. Zhong, G. Ma, Y. Zhou, Y. Shen, H. Ding, and Y. Huang, "Recent progress on advanced imaging techniques for lithium-ion batteries." *Adv. Energy Mater.*, **11**, 2000806 (2021).
- R. F. Ziesche, T. M. Heenan, P. Kumari, J. Williams, W. Li, M. E. Curd, T. L. Burnett, I. Robinson, D. J. Brett, and M. J. Ehrhardt, "Multi-dimensional characterization of battery materials." *Adv. Energy Mater.*, **13**, 2300103 (2023).
- A. Krizhevsky, I. Sutskever, and G. E. Hinton, "Imagenet classification with deep convolutional neural networks." *Advances in Neural Information Processing Systems 25 (NIPS 2012)*, **25** (2012).
- A. Pfirang, S. Didas, and G. Tsotridis, "X-ray computed tomography of gas diffusion layers of PEM fuel cells: segmentation of the microporous layer." *J. Power Sources*, **235**, 81 (2013).
- A. D. Shum, C. P. Liu, W. H. Lim, D. Y. Parkinson, and I. V. Zenyuk, "Using machine learning algorithms for water segmentation in gas diffusion layers of polymer electrolyte fuel cells." *Transp. Porous Media*, **144**, 715 (2022).
- A. Grießer, R. Westerteiger, E. Glatt, H. Hagen, and A. Wiegmann, "Deep learning based segmentation of binder and fibers in gas diffusion layers." *Next Materials*, **6**, 100411 (2025).
- S.-H. Yang et al., "Sparse section imaging-based deep learning electron tomography of porous carbon supports in proton exchange membrane fuel cells." *Journal of Energy Chemistry*, **104**, 795 (2025).
- S.-H. Yang, E.-B. Park, S. Y. Cho, Y. S. Kang, H.-A. Ju, Y. Jeon, D. Yang, S.-D. Yim, S. Lee, and Y.-M. Kim, "Deep learning morphological distribution analysis of metal alloy catalysts in proton exchange membrane fuel cells." *Materials Today Energy*, **36**, 101348 (2023).
- H.-B. Lee et al., "Deep learning image segmentation for the reliable porosity measurement of high-capacity Ni-based oxide cathode secondary particles." *Journal of Analytical Science and Technology*, **14**, 47 (2023).
- C. A. Schneider, W. S. Rasband, and K. W. Eliceiri, "NIH Image to ImageJ: 25 years of image analysis." *Nat. Methods*, **9**, 671 (2012).
- M. Arzt, J. Deschamps, C. Schmied, T. Pietzsch, D. Schmidt, P. Tomancak, R. Haase, and F. Jug, "LABKIT: labeling and segmentation toolkit for big image data." *Frontiers in Computer Science*, **4**, 777728 (2022).
- Ö. Çiçek, A. Abdulkadir, S. S. Lienkamp, T. Brox, and O. Ronneberger, "3D U-Net: learning dense volumetric segmentation from sparse annotation." *Medical Image Computing and Computer-Assisted Intervention-MICCAI 2016: 19th International Conference (Springer)* 424 (2016).
- S. Xie, R. Girshick, P. Dollár, Z. Tu, and K. He, "Aggregated residual transformations for deep neural networks." *Proceedings of the IEEE Conference on Computer Vision and Pattern Recognition* 1492 (2017).
- F. Milletari, N. Navab, and S.-A. Ahmadi, "V-net: fully convolutional neural networks for volumetric medical image segmentation." *2016 Fourth International Conference on 3D Vision (3DV)* (Ieee) 565 (2016).

44. Y.-Q. Yang, Y.-X. Guo, J.-Y. Xiong, Y. Liu, H. Pan, P.-S. Wang, X. Tong, and B. Guo, "Swin3d: A pretrained transformer backbone for 3d indoor scene understanding." *Computational Visual Media*, **11**, 83 (2023).
45. J. T. Gostick, Z. A. Khan, T. G. Tranter, M. D. Kok, M. Agnaou, M. Sadeghi, and R. Jervis, "PoreSpy: a python toolkit for quantitative analysis of porous media images." *Journal of Open Source Software*, **4**, 1296 (2019).
46. E. Erdim, Ö. Akgiray, and İ. Demir, "A revisit of pressure drop-flow rate correlations for packed beds of spheres." *Powder Technol.*, **283**, 488 (2015).
47. J. Gostick, M. Aghighi, J. Hinebaugh, T. Tranter, M. A. Hoeh, H. Day, B. Spellacy, M. H. Sharqawy, A. Bazylak, and A. Burns, "OpenPNM: a pore network modeling package." *Comput. Sci. Eng.*, **18**, 60 (2016).
48. W. J. Schroeder, L. S. Avila, and W. Hoffman, "Visualizing with VTK: a tutorial." *IEEE Comput. Graphics Appl.*, **20**, 20 (2000).
49. V. Berejnov, M. Saha, D. Susac, J. Stumper, M. West, and A. P. Hitchcock, "Advances in structural characterization using soft X-ray scanning transmission microscopy (STXM): mapping and measuring porosity in PEM-FC catalyst layers." *ECS Trans.*, **80**, 241 (2017).
50. Y. V. Yakovlev, Y. V. Lobko, M. Vorokhta, J. Nováková, M. Mazur, I. Matolínová, and V. Matolín, "Ionomer content effect on charge and gas transport in the cathode catalyst layer of proton-exchange membrane fuel cells." *J. Power Sources*, **490**, 229531 (2021).
51. T. Seip, J. K. Lee, M. Ge, W.-K. Lee, N. Shaigan, M. Dinu, K. Fatih, and A. Bazylak, "Stochastic generation of electrolyzer anode catalyst layers." *Electrochim. Acta*, **462**, 142701 (2023).
52. U. U. Ince, H. Markötter, N. Ge, M. Klages, J. Haußmann, M. Göbel, J. Scholta, A. Bazylak, and I. Manke, "3D classification of polymer electrolyte membrane fuel cell materials from in situ X-ray tomographic datasets." *Int. J. Hydrogen Energy*, **45**, 12161 (2020).
53. M. Göbel, M. Godehardt, and K. Schladitz, "Multi-scale structural analysis of gas diffusion layers." *J. Power Sources*, **355**, 8 (2017).
54. I. C. Okereke, M. S. Ismail, D. B. Ingham, K. Hughes, L. Ma, and M. Pourkashanian, "Single- and double-sided coated gas diffusion layers used in polymer electrolyte fuel cells: a numerical study." *Energies*, **16**, 4363 (2023).
55. C. Lin, K. Cheng, S. Li, S. Ouyang, Y. Wang, and M. Pan, "High-flux microporous layers with bimodal pore structures for proton exchange membrane fuel cells." *ACS Omega*, **10**, 19966 (2025).
56. A. Ozden, S. Shahgaldi, J. Zhao, X. Li, and F. Hamdullahpur, "Assessment of graphene as an alternative microporous layer material for proton exchange membrane fuel cells." *Fuel*, **215**, 726 (2018).
57. H. Markötter, J. Haußmann, R. Alink, C. Tötze, T. Arlt, M. Klages, H. Riesemeier, J. Scholta, D. Gerteisen, and J. Banhart, "Influence of cracks in the microporous layer on the water distribution in a PEM fuel cell investigated by synchrotron radiography." *Electrochem. Commun.*, **34**, 22 (2013).
58. C. H. Chen, K. Khedekar, A. Zaffora, M. Santamaria, M. Coats, S. Pylypenko, P. A. García-Salaberri, J. Braaten, P. Atanasov, and N. Tamura, "Effect of microporous layer cracks on catalyst durability of polymer electrolyte fuel cells for heavy-duty applications." *ACS Appl. Energy Mater.*, **7**, 5736 (2024).
59. H. Tang, S. Wang, M. Pan, and R. Yuan, "Porosity-graded micro-porous layers for polymer electrolyte membrane fuel cells." *J. Power Sources*, **166**, 41 (2007).
60. C. Zhao, H. Zhang, Z. Huang, M. Zhao, H. Chen, and G. Lin, "Two-stage microporous layers with gradient pore size structure for improving the performance of proton exchange membrane fuel cells." *Polymers*, **15**, 2740 (2023).
61. D. Alvarez, "JUWELS cluster and booster: exascale pathfinder with modular supercomputing architecture at juelich supercomputing centre." *Journal of Large-Scale Research Facilities*, **7**, A183 (2021).